

Theoretical investigation of mechanical, thermodynamical, electronic and transport properties of Ni₂P

Y. Bendakmousse

*Département de Physique & Laboratoire d'études Physico-chimiques des Matériaux, Faculté des Sciences de la matière, Université de Batna 1, Batna, 05000, Algérie.
e-mail: yacine.bendakmousse@univ-batna.dz*

N. Baadji

*Département de Physique & Laboratoire de Physique des Matériaux et ses applications, Faculté des Sciences, Université Mohamed Boudiaf, M'sila, 28000, Algérie.
e-mail: nadjib.baadji@univ-msila.dz*

K. Zanat

*Laboratoire de Physique, Université 8 Mai 1945, BP 401, 24000 Guelma, Algeria.
e-mail: zanat.k@gmail.com*

Received 8 May 2024; accepted 4 February 2025

The all-electron full-potential linearized augmented plane-wave method is used to investigate the structural, electronic, and thermodynamic properties of the hexagonal structure of Ni₂P. We show that Ni₂P is stable and has interesting mechanical and thermodynamical properties. While we used the non-equilibrium Green's function formalism to investigate electronic transport properties, particularly conductance by constructing a symmetric junction with Ni₂P acting as the spacer between two gold electrodes (Au/Ni₂P/Au). We considered both phosphorus-rich and phosphorus-poor terminated interface and we show that the transmission coefficients depends on the nature of Ni₂P/Au interface. Furthermore, we mimic experimental junction, by analyzing the impact of phosphorus deficiency. We show that Ni₂P's conductance is altered differently depending on whether the defect is located at the interface or deep within the spacer.

Keywords: Nickel phosphide; electronic transport; DFT; NEGF.

DOI: <https://doi.org/10.31349/RevMexFis.71.040501>

1. Introduction

Hydrogen fuel, produced through water electrolysis, emerges as a promising clean energy alternative to fossil fuels [1]. The electrocatalytic hydrogen evolution reaction (HER) represents a crucial step in water electrolysis, with platinum (Pt) currently recognized as the most efficient HER electrocatalyst, exhibiting a nearly zero onset overpotential [2]. However, due to its high cost and limited availability, extensive research has been dedicated to identifying low-cost and catalytically active alternatives. Transition metal phosphides (TMP) have emerged as promising candidates due to their distinct and unique catalytic properties, offering potential solutions for energy production and storage systems [3].

Nickel phosphide (Ni-P) is distinguished among transition metal phosphides due to its catalytic and electrochemical characteristics, particularly in alkaline electrolyzers and fuel cells. It has demonstrated notable performance in both the hydrogen evolution (HER) and oxygen evolution reactions (OER). Nickel phosphide catalysts exhibit high activity, stability, and potential for large-scale production [4]. Moreover, Ni-P has gathered attention for its potential in energy storage applications, particularly rechargeable batteries. Recently, its effectiveness as an electrode material have been demonstrated, especially as an anode in lithium-ion batter-

ies, where nickel phosphide electrodes have shown impressive cycling stability and high specific capacity, critical for efficient energy storage [5-7].

Of the nine intermetallic Ni-P phases [8-10], Ni₂P is one of the most prominent compounds. Recently, Wei *et al.* [11] have theoretically demonstrated that the Ni₂P (001) surface exhibits excellent performance in catalyzing the hydrodesulfurization (HDS) process and that the bulk Ni₂P presents a real-space topological ferroelectricity [12].

For Ni₂P to perform optimally in catalysis and in rechargeable batteries, it must possess stable mechanical and electrical properties [13]. Hence, there is a need for a comprehensive understanding of its mechanical and electrical properties, which, to our knowledge, are insufficiently explored. To address this gap, we aim to investigate the mechanical, thermodynamic, and transport properties of Ni₂P through first-principles calculations within the density functional theory (DFT) framework combined with non-equilibrium Green's function (NEGF).

2. Computation details

The geometrical, electronic, and thermodynamic properties of Ni₂P's hexagonal structure were calculated using the all-electron full-potential linear augmented plane-wave

(FLAPW) method [14,15] implemented in the Fleur code [16]. The calculations were conducted within the Perdew, Burke, and Ernzerhof (PBE) parametrization of the generalized gradient approximation for the exchange-correlation potential [17]. A muffin-tin radius of 2.03 Bohr has been considered for both Ni and P atoms. We used $16 \times 16 \times 20$ k-points in the Brillouin zone, generated using the Monkhorst-Pack scheme [18], for electronic and mechanical properties. However, a finer mesh of 24600 k-points ($40 \times 40 \times 60$) in the irreducible Brillouin has been used to plot the Fermi surface and to calculate the electron's group velocity (See in Fig. 3). In contrast, the linear tetrahedron method is adopted for the integration in the Brillouin zone (BZ) to calculate the density of states (DOS) [19]. For the transport calculation through Ni₂P-based junctions, we employed the non-equilibrium Green's function [20] as implemented in the Smeagol [21,22] based on the SIESTA-DFT packages [23]. A uniform real space grid with a cutoff of 400 Ry is used in these calculations. We used norm-conserving, fully separable Troullier Martin pseudopotentials [24] and double-zeta ζ (DZ) as the basis set. A fine k-point Monkhorst-Pack mesh (32×32) was used to sample the 2d Brillouin zone to evaluated both density matrix and the transmission coefficient. A denser set, of 128×128 k-points, was used to obtain the value of the transmission coefficient at the Fermi level.

3. The mechanical properties

Ni₂P assumes a hexagonal structure belonging to the revised C22 (Fe₂P) structure type (see Fig. 1), with a space group $P\bar{6}2m$. The six Ni atoms occupy the Wyckoff positions 3(f) and 3(g) (hereafter denoted as Ni(f) and Ni(g), respectively), while phosphorus atoms occupy the 2(c) and 1(b) Wyckoff positions. In the $P\bar{6}2m$ space group (number 189), the Wyckoff 3(f) and 3(g) positions correspond to fractional coordinates x_f at x_g . Consequently, the structure of the Ni₂P can

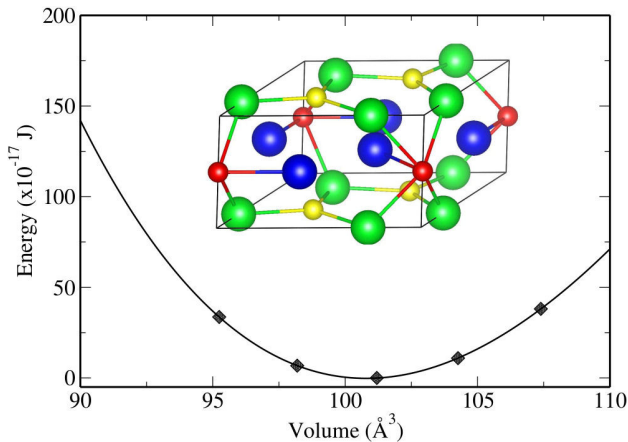


FIGURE 1. (Color online) The crystalline structure of Ni₂P is depicted, with Ni(f) atoms shown in green and Ni(g) atoms presented in blue. The variation of total energy as a function of volume under isotropic deformation with c/a held constant (by diamonds), fitted with the Birch-Murnaghan equation of state (solid line).

TABLE I. Calculated optimum lattice parameters (a and c) and fractional coordinates, x_f and x_g of Wyckoff positions 3(f) and 3(g), respectively, of the hexagonal structure of Ni₂P system compared experimental values and other calculations.

Lattice parameters		x_f	x_g	Reference
a_0	c			
5.885	3.373	0.2596	0.6012	this work
5.859	3.382	0.2575	0.5957	exp [29]
5.879	3.373	-	-	[30]

visualized as an alternation of two nonequivalent atomic plans along the (0001) direction with stoichiometry of Ni₃P₂ and Ni₃P. Theoretical studies [25] have demonstrated that the Ni₃P₂-terminated surface is energetically favored compared to the Ni₃P-terminated surface. Additionally, the catalytic activity strongly depends on the nature of the Ni₂P surface [26]. This difference between the terminated surfaces will be further investigated during the transport analysis in the last section. Furthermore, Wei *et al.* [12] reported that the metallic and non-centrosymmetric Ni₂P exhibits real-space topological ferroelectricity, with the polyhedral polarity being reversed under an applied in-plane compressive strain. This indicates that mechanical properties play a major role and must be taken into account.

We begin by calculating the optimum lattice parameters a and c , as well as the equilibrium positions of Ni(f) and Ni(g) atoms. The obtained values are listed in Table I and compared to experimental and other calculated values. The corresponding optimum volume is then used to calculate the isotropic bulk modulus and its pressure derivative by fitting the variation of the total energy as a function of volume (see Fig. 1) with the Birch-Murnaghan equation of state [27,28].

Furthermore, we assess the stability of the hexagonal structure by calculating the elastic constant tensor, which describes how a material responds to deforming forces. These constants are usually determined either from the stress-strain or energy-strain relationship. The former approach relies on highly accurate calculations and requires denser k-point meshes. That's why, in this study, we adopt for the latter approach. For the hexagonal structure, five independent elastic constants [31] can be obtained by subjecting the lattice to small distortions [32]. We applied a lattice distortion ($\delta = \pm 1, \pm 2$) analogous to that of Fast *et al.* [33]. The results were fitted with a parabolic equation to determine the elastic constants. The obtained values, in GPa, are as follows: $C_{11} = 300.53$, $C_{12} = 162.70$, $C_{13} = 181.62$, $C_{33} = 244.53$, and $C_{44} = 29.71$. These values are in good agreement with those reported by [30]. It's important to note that in our simulations, ions are kept frozen while only lattice deformation is applied. As a result, the obtained elastic constants are relatively higher compared to other reported values. Nonetheless, in both scenarios, the values of C_{ij} satisfy the mechanical stability criterion for the hexagonal structure [34]. In addi-

tion, the dynamical stability can be checked from the phonon dispersion and it was calculated by Zhao *et al.* [30]. The obtained C_{ij} values can be used to calculate the isotropic bulk modulus under the assumption that the ratio c/a remains unchanged when the lattice is subjected to isotropic stress [35]. We have:

$$B_{\text{iso}} = \frac{2}{9}(C_{11} + C_{12} + 2C_{13} + C_{33}/2).$$

We obtain $B_{\text{iso}} = 210.83$ GPa. This value can be compared with the bulk modulus obtained from fitting the energy variation versus volume using the Birch-Murnaghan equation of state (See Fig. 1). The fit yields $B = 199.57$ GPa, with a pressure derivative $B' = 4.57$. Thus, the value is in an agreement with that obtained from our calculated elastic constants and other calculations [30].

Similarly, we obtained the isotropic shear modulus with a value of:

$$G = \frac{1}{30}(7C_{11} - 5C_{12} + 12C_{44} + 2C_{33} - 4C_{13}).$$

We get $G = 46.98$ GPa very close to that obtained with VASP code [30]. In addition, We can calculate the averaged Young's modulus (E) and the averaged Poisson's ratio (ν) of Ni₂P starting the bulk and shear modulus from the following relations [36]:

$$E = \frac{9BG}{3B + G}, \quad \nu = \frac{3B - 2G}{6B + 2G}.$$

An averaged Young's modulus $E = 67.95$ GPa and the averaged Poisson's ratio $\nu = 0.396$ are obtained which compared very well to previously calculated values [30].

Moreover, the ductility or brittleness behavior can be characterized using Poisson's ratio (ν) according to Frantsevich *et al.* [37], $\nu < 1/3$ for brittle materials and $\nu > 1/3$ for ductile materials. From the obtained value of ν , we conclude that the compound Ni₂P is ductile.

One important material characteristic that can be calculated based on elastic constants is the Debye temperature, represented by the following equation [38]:

$$\theta_D = \frac{h}{k_B} \left(\frac{3nN_A\rho}{4\pi M} \right)^{1/3} v_m.$$

In this expression, h , k_B , and N_A are Planck's, Boltzmann's, and Avogadro's constant, respectively. ρ is the density of the material and M is its molar mass, n is the total number of atoms per formula (here is 3), and v_m is the averaged elastic wave velocity. This equation is usually hindered by the problem of calculating v_m . For each direction in a crystal, there exist three velocities, each of which is a complex function of elastic constants, propagation direction. The expression for the averaged speed velocity, as given by

$$v_m = \left[\frac{1}{3} \sum_{i=1}^3 \int_V \frac{1}{v_i^3} \frac{d\Omega}{4\pi} \right]^{-\frac{1}{3}}.$$

Furthermore, the relationship between the stiffness tensor and sound velocities in a solid enables the determination of (pseudo) longitudinal and transverse velocities of sound (v_i) by solving the Christoffel equation, as given by Ref. [41]:

$$\sum_{ij} \left[\hat{M}_{ij} - \rho\omega^2\delta_{ij} \right] s_{ij} = 0.$$

Here, ω is the frequency and \hat{M} is the Christoffel matrix, defined as

$$\hat{M}_{ij} = \sum_{nm} q_n C_{inmj} q_m.$$

From the three obtained eigenvalues $\omega^2(q)$, three phase-velocities are derived: one primary (v_P) and two secondary (v_S^1, v_S^2), corresponding to (pseudo-) longitudinal and (pseudo) transverse polarizations (eigenvectors), respectively. Each of these velocities depends on the propagation direction q_i , characterized by angle θ and ϕ . The above double-integral is computed using Simpson's 1/3 rule with a 360×720 mesh for the angles θ and ϕ , respectively. We obtain $v_m = 2.741$ km/s.

Alternatively, the primary and secondary isotropic sound velocities can be calculated using :

$$v_S^{\text{iso}} = \sqrt{\frac{G}{\rho}}, \quad v_P^{\text{iso}} = \sqrt{\frac{3B + 4G}{3\rho}}.$$

Here, B and G represent the bulk modulus and shear modulus, respectively, which have been calculated beforehand. These velocities are then used to calculate v_m [38] as :

$$\frac{3}{(v_m^{\text{iso}})^3} = \frac{1}{(v_P^{\text{iso}})^3} + \frac{2}{(v_S^{\text{iso}})^3}.$$

We calculated the isotropic primary and secondary speeds of sound as $V_{\text{iso}}^P = 6.119$ km/s and $V_{\text{iso}}^S = 2.536$ km/s, respectively, resulting in the averaged isotropic speed of sound $v_m^{\text{iso}} = 2.870$ km/s which is slightly bigger than v_m obtained by the integral. These values of the averaged elastic wave velocity lead to a Debye's temperature $\Theta_D = 364.3$ K and $\Theta_D^{\text{iso}} = 381.4$ K, respectively, which are in good agreement with the Debye temperature value at [42].

Additionally, the Debye temperature allows us to calculate the ionic contribution to the heat capacity (C_P^i) given by (see [43])

$$C_P^i = \beta T^3 \quad \beta = \frac{12\pi^4 N k_B}{5\Theta_D^3},$$

where β is the coefficient of the Debye lattice heat capacity at low T and we obtain $\beta = 0.12$ mJ/mol.K⁴.

To find the total heat capacity one needs to calculate the electronic contribution as well (C_P^e) which is related to the density of state at the Fermi level through the relation (see [44]) :

$$C_P^e = \gamma T \quad \gamma = \frac{\pi^2}{3} D(E_F) k_B^2,$$

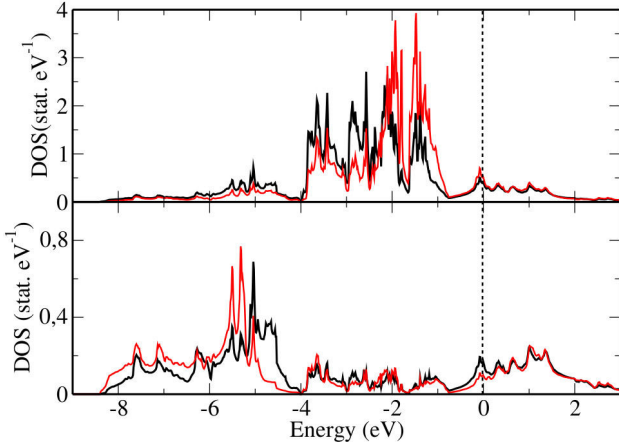


FIGURE 2. (Color online) Atomic-resolved density of states of Ni and P atoms in Ni_3P_2 (black lines) and Ni_3P_1 (red lines) planes. Fermi level is indicated by vertical dashed line.

where γ is the Sommerfeld constant and $D(E_F)$ is the density of states at the Fermi level. From the density of states (presented in Fig. 2), which have a finite density of state around the Fermi level (2.34 state/eV.fu) confirming the metallic nature of Ni_2P , we get a value of $\gamma = 5.52 \text{ mJ/mol.K}^2$.

Therefore, the heat capacity at low temperatures (by combining the calculated elastic and electronic parameters) is given by the following relationship [41]:

$$C_p = \gamma T + \beta T^3.$$

4. Electronic properties

The revised C_{22} structure of Ni_2P can be visualized as alternating Ni_3P_2 and Ni_3P planes along the c -axis. This structural arrangement can significantly influence both catalytic activity and transport properties, depending on the terminated surface. To illustrate this effect, we present the atomic-resolved density of states (DOS) for both Ni and P in both planes, as depicted in Fig. 2. Below the Fermi level, the density of states is primarily attributed to the d-orbitals of Nickel atoms, while at lower energies, it results from the p-orbitals of phosphorus. Around the Fermi level, the density of states results from the hybridization of both phosphorus p-orbitals and nickel d-orbitals. At the Fermi level, the density of states results from the contributions of both the d-orbitals of Ni (f) and Ni (g) as well as the p-orbitals of phosphorus, with Ni(f) exhibiting a slightly higher contribution (Ni in the P-rich plane). The contribution of the p-orbitals of phosphorus in the Ni_3P_2 plane is higher than that in the Ni_3P plane. This suggests a stronger bonding between phosphorus and nickel in the Ni_3P_1 plane due to the trivalency of phosphorus, resulting in an additional charge in the Ni_3P_2 plane. This disparity in the contributions to the density of states at the Fermi level will lead to differences in reactivity and transport properties.

We emphasize that relying solely on the density of states at the Fermi level is insufficient to adequately describe the

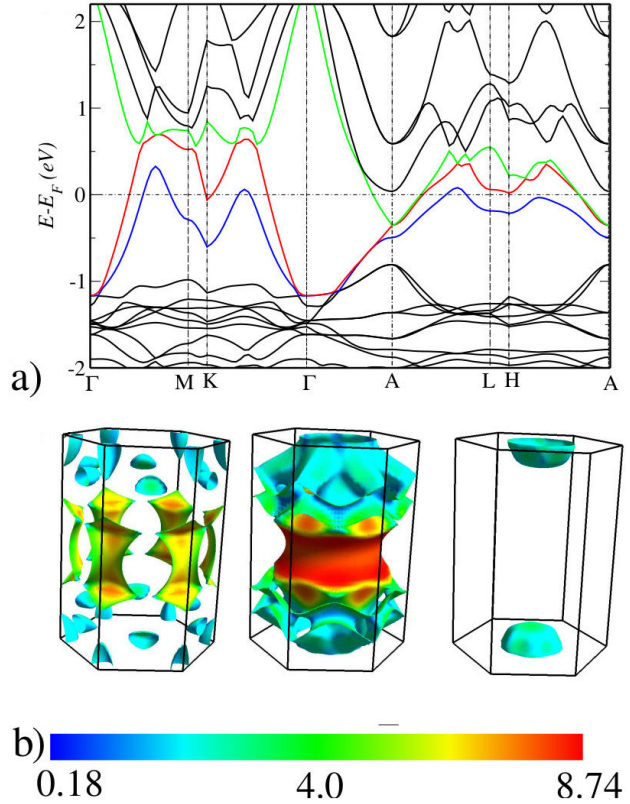


FIGURE 3. (Color online) (a) Ni_2P 's energy band structure along high-symmetry lines, (b) Band's contributions to the Fermi surface with their corresponding speeds represented by a color code.

conductivity of Ni_2P ; it merely indicates its conductive nature. To gain further insight into the conductivity of Bulk Ni_2P , which relies on the density of states at the Fermi level and, more importantly, on the speed of electrons extracted from the energy dispersion $v_{k\alpha} = \partial\varepsilon(\vec{k})/\partial k_\alpha$. In the context of the relaxation time approximation and the Linear Boltzmann Equation, conductivity ($\sigma_{\alpha,\beta}$) is given by the expression [45]:

$$\sigma_{\alpha,\beta} = \frac{e^2}{4\pi} \sum_n \int d^3k \tau v_\alpha(\vec{k}) v_\beta(\vec{k}) \left(-\frac{\partial f}{\partial \varepsilon} \right).$$

Here, the sum is taken over all energy bands. The derivative of the Fermi-Dirac distribution function (f) ensures that only electrons near the Fermi level contribute to conductivity. At low temperatures ($T \ll T_F$), it can be demonstrated that conductivity scales proportionally to the Fermi surface area (S_F) and the Fermi velocity (v_F), *i.e.*, $\sigma \propto S_F v_F$. For the energy dispersion, we plot the energy band structure on Ni_2P in Fig. 3a) along high-symmetry lines of its hexagonal Brillouin zone. The band structure reveals three bands crossing the Fermi level (represented by blue, red, and green lines). In addition, the contribution of each of these bands to the Fermi surface, along with their corresponding speeds represented by a color code on the Fermi surface, are depicted in Fig. 3b).

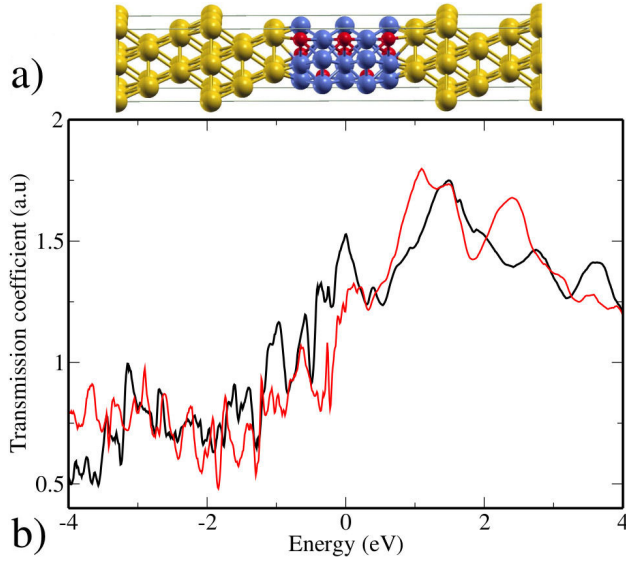


FIGURE 4. a) The atomic geometry of the Au-Ni₂P-Au system with five Ni₂P layers. b) the computed transmission coefficient of junctions with different interfaces: Ni₃P₂ (Black) and Ni₃P₁ (red), using density functional theory and NEGF formalism.

5. Transport properties

To go beyond the limitation of the relaxation time approximation and to probe the effect of the surface termination of Ni₂P on the transport properties, we adopt the Landauer-Buttiker approach [46,47], by constructing symmetrical junctions made of two gold electrodes separated by 5 layers of Ni₂P [see Fig. 4a)]. We chose gold since the in-plane optimum lattice parameter, calculated in the previous sections, matches the Au parameter $a_0 = \sqrt{2}a_{Au}$, which is essential for the layer-by-layer growth of Ni₂P on the (111) surface of gold. We thus use $a_0 = 5.885 \text{ \AA}$ as the in-plane lattice parameter for the Au/Ni₂P/Au(111) junctions. Additionally, we maintain a fixed distance between gold and Ni₂P planes, regardless of the interface's characteristics, and it is set to a value of 2.044 \AA . However, the intra-plane distances in the gold electrodes and Ni₂P spacer remain consistent with their respective bulk values (2.404 \AA and 1.686 \AA respectively).

As discussed earlier, Ni₂P can be viewed as alternating planes of Ni₃P₂ (phosphorus-rich) and Ni₃P₁ (phosphorus-poor), we examined both interfaces: Au/Ni₃P₂ and Au/Ni₃P₁. The calculated transmission coefficients are presented in Fig. 4. Below the Fermi level of the gold electrode (taken as an energy reference), the transmission coefficients for both interfaces are low and increase above the Fermi level. At the Fermi level, the phosphorus-rich terminated interface (Ni₃P₂) exhibits higher transmission and thus higher conductivity compared to the phosphorus-poor interface (Ni₃P₁). This enhanced transmission is attributed to the hybridization between gold and phosphorus orbitals, resulting from the additional charge discussed in the previous section. Specifically, in the case of the P-rich interface, there is notable hybridiza-

tion between the gold orbitals and the Ni₂P orbital, particularly with the third band, which is predominantly associated with P (as shown in Fig. 3). This hybridization results in higher transmission around the Γ point.

The ideal structure of the sample cannot be achieved experimentally. To mimic experimental junctions, which usually display some disorder and roughness at the interface or deep in the junction, we calculate the transmission coefficient for a junction with a P-rich interface with defects. In the first case, the defect results from a missing P at one of the interfaces, while in the second case, the missing P is in the middle of the junction.

Figure 5 presents the calculated transmission coefficients for both cases compared to the ideal interface (P-rich interface). It shows that the defect causes a drop in the conductance in both cases. The defect in the middle of the junction leads to a larger decrease in the conductance by about 20%, resulting in increased resistivity and thus higher energy consumption.

To get more insight into the transport properties, we plot the total density of states of the clean and defected junctions around the Fermi level of the electrode (see Fig. 5). First, at energies 2 to 4 eV below the Fermi, where the density of the bulk is higher, the transmission coefficient is reduced. This is

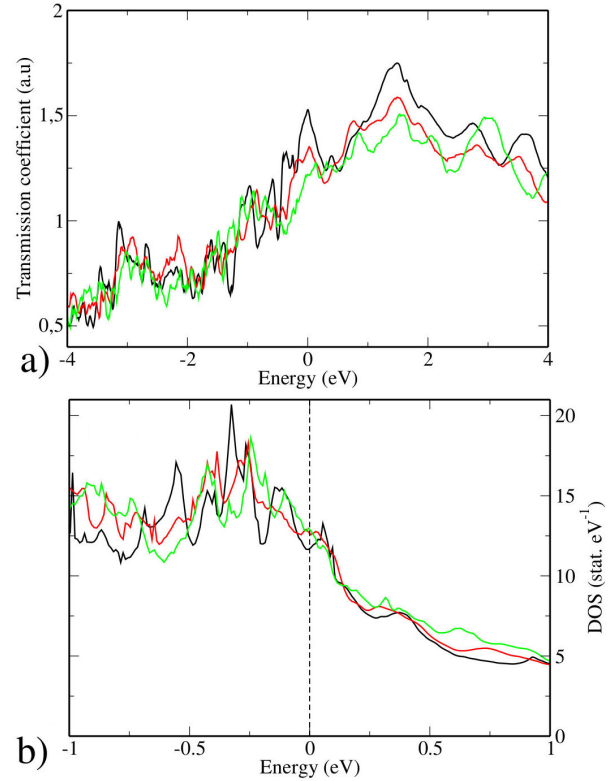


FIGURE 5. Variation of a) transmission coefficients and b) total density of states of the spacer (NiP), for clean junction (black line) and defected junctions with a missing P at the interface and in the middle of the spacer, red and green lines respectively.

because, at this energy range, the main contribution comes from the d-orbital of Ni, as discussed above, and these orbitals are less extended compared to s and p orbitals. Around the Fermi level, the total density of states of the defective spacer is slightly higher than that of the clean junction. It is the opposite of the trend of the transmission coefficient since the electrons have a lower speed in the defective spacers, and thus a low probability of transmission.

6. Conclusions

Transition metal phosphides have emerged as promising candidates due to their distinct and unique catalytic properties, offering potential solutions for energy production and storage systems. Ni₂P is considered promising in the fields of dynamic catalysis as a cheap alternative to platinum due to its catalytic and electrochemical properties. In this context, structural, electronic, and thermodynamic properties of Ni₂P's hexagonal structure has been studied in ab-initio manner using the all-electron full-potential linear augmented

plane-wave method combined with NEGF technique for transport properties. The results show that the Ni₂P structure is stable under severe conditions, such as high pressure and temperature. The structure of Ni₂P consists of alternating planes rich and poor in phosphorus, which have different conductive properties. When Ni₂P structure is used in real junctions, different termination interfaces will occur displaying some disorder and roughness at the interface or deep in the junction. This experimental situation has been simulated by considering Ni₂P as a spacer between two gold electrodes (Au/Ni₂P/Au) with two possible terminated interfaces, rich (Ni₃P₂) and poor (Ni₃P₁) in phosphorus. In addition, both pristine and defective junction, with missing phosphorus atom at the interface and in the middle of the spacer, has also been considered. Our calculations of the transmission coefficient show that interfaces enriched with phosphorus in the simulated systems exhibit higher conductivity. Conversely, any phosphorus deficiency leads to reduced conductivity and thus higher energy consumption. Nevertheless, Ni₂P retains its metallic character in all cases.

-
1. P. J. Megía, A. J. Vizcaíno, J. A. Calles, and A. Carrero, *Energy & Fuels* 35, 16403 (2021), <https://doi.org/10.1021/acs.energyfuels.1c02501>
 2. S. Wang, A. Lu, and C.-J. Zhong, *Nano Convergence* 8 (2021) 4.
 3. J. Theerthagiri *et al.*, *Ceramics International* 47, 4404 (2021), ISSN 0272-8842,
 4. C. Hu, C. Lv, S. Liu, Y. Shi, J. Song, Z. Zhang, J. Cai, and A. Watanabe, *Catalysts* 10 (2020), ISSN 2073-4344, <https://www.mdpi.com/2073-4344/10/2/188>
 5. H. Sun, X. Xu, Z. Yan, X. Chen, F. Cheng, P. S. Weiss, and J. Chen, *Chemistry of Materials* 29, 8539 (2017).
 6. Y. Li, J. Zhang, D. Li, J. Ding, Y. Liu, and Q. Cai, *ChemElectroChem* 6, 5492 (2019).
 7. F. Fu, Q. He, X. Zhang, J. Key, P. Shen, and J. Zhu, *Batteries* 9 (2023), ISSN 2313-0105, <https://www.mdpi.com/2313-0105/9/5/267>
 8. K. Lee and P. Nash, *Phase diagrams of binary nickel alloys*. Materials Park, OH: ASM International pp. 235-246 (1991).
 9. S. Orishchin, V. Babizhetskii, and Y. B. Kuz'ma, *Crystallography Reports* 45 (2000).
 10. S. Rundqvist, *Acta Chemica Scandinavica* 4, 992 (1962).
 11. Q. Wei, X. Liu, Y. Zhou, Z. Xu, P. Zhang, and D. Liu, *Catalysis Today* 353, 39 (2020), ISSN 0920-5861, international Symposium on Advances in Hydroprocessing of Oil Fractions (ISA-HOF 2019),
 12. X.-K. Wei *et al.*, *Advanced materials* 32, 2003479 (2020).
 13. M.-Q. Wang, C. Tang, C. Ye, J. Duan, C. Li, Y. Chen, S.-J. Bao, and M. Xu, *Journal of Materials Chemistry A* 6, 14734 (2018).
 14. M. Weinert, E. Wimmer, and A. J. Freeman, *Phys. Rev. B* 26, 4571 (1982), <https://link.aps.org/doi/10.1103/PhysRevB.26.4571>.
 15. E. Wimmer, H. Krakauer, M. Weinert, and A. J. Freeman, *Phys. Rev. B* 24, 864 (1981), <https://link.aps.org/doi/10.1103/PhysRevB.24.864>
 16. S. Blügel and G. Bihlmayer (John von Neumann Institute for Computing, 2006), vol. 31 of *Computational Nanoscience: Do It Yourself!*, pp. 85-129, ISBN 3-00-017350-1, URL <https://juser.fz-juelich.de/record/50026/files/FZJ-2014-02213.pdf>.
 17. J. P. Perdew, K. Burke, and M. Ernzerhof, *Phys. Rev. Lett.* 77, 3865 (1996), URL <https://link.aps.org/doi/10.1103/PhysRevLett.77.3865>.
 18. H. J. Monkhorst and J. D. Pack, *Physical review B* 13, 5188 (1976).
 19. P. E. Blöchl, O. Jepsen, and O. K. Andersen, *Phys. Rev. B* 49, 16223 (1994), URL <https://link.aps.org/doi/10.1103/PhysRevB.49.16223>.
 20. S. Datta, *Index* (Cambridge University Press, 1995), p. 375-377, *Cambridge Studies in Semiconductor Physics and Microelectronic Engineering*.
 21. A. R. Rocha, V. M. García-Suárez, S. W. Bailey, C. J. Lambert, J. Ferrer, and S. Sanvito, *Nature Materials* 4, 335 (2005), ISSN 1476-4660, <https://doi.org/10.1038/nmat1349>
 22. I. Rungger and S. Sanvito, *Phys. Rev. B* 78 (2008) 035407, <https://link.aps.org/doi/10.1103/PhysRevB.78.035407>
 23. J. M. Soler, E. Artacho, J. D. Gale, A. García, J. Junquera, P. Ordejón, and D. Sánchez-Portal, *Journal of Physics: Condensed Matter* 14 (2002) 2745, <https://dx.doi.org/10.1088/0953-8984/14/11/302>

24. N. Troullier and J. L. Martins, *Phys. Rev. B* **43**, 1993 (1991), <https://link.aps.org/doi/10.1103/PhysRevB.43.1993>
25. G. E. Ayom, M. D. Khan, S. C. Masikane, F. M. de Souza, W. Lin, R. K. Gupta, and N. Revaprasadu, *Sustainable Energy & Fuels* **6**, 1319 (2022).
26. U. Guharoy, T. Ramirez Reina, E. Olsson, S. Gu, and Q. Cai, *ACS Catalysis* **9**, 3487 (2019).
27. F. Birch, *Phys. Rev.* **71**, 809 (1947), <https://link.aps.org/doi/10.1103/PhysRev.71.809>
28. F. D. Murnaghan, *Proceedings of the National Academy of Sciences* **30**, 244 (1944), <https://www.pnas.org/doi/pdf/10.1073/pnas.30.9.244>, <https://www.pnas.org/doi/abs/10.1073/pnas.30.9.244>
29. S. Rundqvist, *Acta Chemica Scandinavica* **4**, 992 (1962).
30. D. Zhao, L. Zhou, Y. Du, A. Wang, Y. Peng, Y. Kong, C. Sha, Y. Ouyang, and W. Zhang, *Calphad* **35**, 284 (2011).
31. J. F. Nye, *Physical properties of crystals: their representation by tensors and matrices* (Oxford university press, 1985).
32. F. Jona and P. M. Marcus, *Phys. Rev. B* **66**, 094104 (2002), <https://link.aps.org/doi/10.1103/PhysRevB.66.094104>
33. L. Fast, J. M. Wills, B. Johansson, and O. Eriksson, *Phys. Rev. B* **51**, 17431 (1995), <https://link.aps.org/doi/10.1103/PhysRevB.51.17431>
34. F. Mouhat and F. m. c.-X. Coudert, *Phys. Rev. B* **90**, 224104 (2014), <https://link.aps.org/doi/10.1103/PhysRevB.90.224104>
35. Z.-j. Wu, E.-j. Zhao, H.-p. Xiang, X.-f. Hao, X.-j. Liu, and J. Meng, *Phys. Rev. B* **76**, 054115 (2007), <https://link.aps.org/doi/10.1103/PhysRevB.76.054115>
36. Z.-j. Wu, E.-j. Zhao, H.-p. Xiang, X.-f. Hao, X.-j. Liu, and J. Meng, *Phys. Rev. B* **76**, 054115 (2007), <https://link.aps.org/doi/10.1103/PhysRevB.76.054115>
37. I. Frantsevich, F. Voronov, and S. Bakuta, *Kiev, Izdatel'stvo Naukova Dumka*, **1982** (1982) 288.
38. O. L. Anderson, *Journal of Physics and Chemistry of Solids* **24** (1963) 909, ISSN 0022-3697,
39. H. Huntington, *Solid state physics*, ed. f. seltz and d. turnball, vol. 7, chap. iii (1958).
40. G. A. ALERS, in *Lattice Dynamics*, edited by W. P. MASON (Academic Press, 1965), vol. 3 of *Physical Acoustics*, pp. 1-42.
41. J. W. Jaeken and S. Cottenier, *Computer Physics Communications* **207**, 445 (2016).
42. Y. Tian and P. Wu, *Journal of Materials Research* **32**, 1 (2017).
43. G. Grimvall, *Thermophysical properties of materials* (Elsevier, 1999).
44. N. W. Ashcroft and N. D. Mermin, *Solid State Physics* (Holt-Saunders, 1976).
45. J. M. Ziman, *Principles of the Theory of Solids* (Cambridge university press, 1972).
46. R. Landauer, *IBM Journal of Research and Development* **1**, 223 (1957).
47. M. Büttiker, *Phys. Rev. Lett.* **65**, 2901 (1990), <https://link.aps.org/doi/10.1103/PhysRevLett.65.2901>.